The Anion of Oxalyl Chloride: Structure and Spectroscopy

Yerbolat Dauletyarov, Beverly Ru, and Andrei Sanov *

Department of Chemistry and Biochemistry, University of Arizona, Tucson, Arizona 85721, USA

ABSTRACT

The structure and spectroscopy of the anion of oxalyl chloride are investigated using photoelectron imaging experiments and ab initio modeling. The photoelectron images, spectra, and angular distributions are obtained at 355 nm and 532 nm wavelengths. The 355 nm spectrum consists of a band assigned to a transition from the ground state of the anion to the ground state of the neutral. Its onset at ~1.8 eV corresponds to the adiabatic electron affinity (EA) of oxalyl chloride, in agreement with the coupled-cluster calculations predicting an EA of 1.797 eV. The observed vertical detachment energy, 2.33(4) eV, is also in agreement with the theory predictions. The 532 nm spectrum additionally reveals a sharp onset near the photon-energy limit. This feature is ascribed to autodetachment via a low-energy anionic resonance. The results are discussed in the context of the substitution series, which includes glyoxal, methylglyoxal (single methyl substitution), biacetyl (double methyl substitution), and oxalyl chloride (double chlorine substitution). The EAs and anion detachment energies follow the trend: Biacetyl < Methylglyoxal < Glyoxal << Oxalyl Chloride. The electron donating character of the methyl group has a destabilizing effect on the substituted anions, reducing the EA from glyoxal to methylglyoxal to biacetyl. In contrast, the strong electron-withdrawing (inductive) power of Cl lends additional stabilization to the oxalyl chloride anion, resulting in a large (~1 eV) increase in its detachment energy, compared to glyoxal.

1. INTRODUCTION

Oxalyl chloride, $(COCl)_2$ is a versatile organic reagent, widely used in chlorination, oxidation, reduction, dehydration, decarboxylation, and formylation reactions.[1] It is related and often compared to phosgene, $COCl_2$, but this work pursues an alternative perspective viewing oxalyl chloride as a member of the substituted-glyoxal family (see Scheme 1).

Scheme 1. Lewis Structures of Glyoxal, Methylglyoxal, Biacetyl, and Oxalyl Chloride.

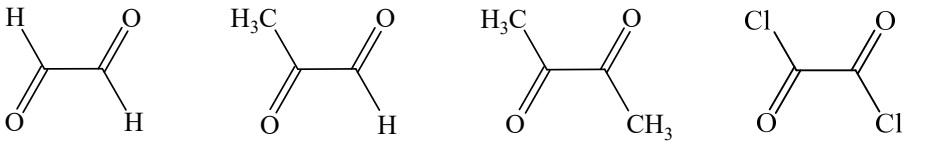

Glyoxal Methylglyoxal Biacetyl Oxalyl Chloride

Despite the structural and photochemical properties of oxalyl chloride that pique a physical chemist's interest, the spectroscopic literature on this molecule and especially its anion is sparse. This is due in part to the dangerous properties of this compound. In the experiment by Chu et al.,[2] parent and fragment cation yields for oxalyl chloride were measured using synchrotron radiation, allowing the authors to estimate that *anti* and *gauche* were the two conformers present in the gas phase (~70% and ~30%, respectively), with no contribution from the *syn* conformer. A valence-shell photoelectron spectrum of neutral oxalyl chloride in the photon energy range 19-91 eV was reported recently by Holland et al.[3] There have been several determinations of the ionization energy, 10.91(5) eV adiabatic value.[4-5] Below the ionization threshold, the UV/VIS absorption spectrum of oxalyl chloride shows an onset at about 390 nm.[6-8] In 1997, Suits and co-workers exploited one feature of the absorption spectrum to study the gas-phase photochemistry of oxalyl chloride near 235 nm. Using photofragment ion imaging, they discovered that the $(COCl)_2$ molecule dissociates into four fragments following the absorption of just one UV photon.[9]

In the present work, we focus on the anion of oxalyl chloride. There is currently a dearth of

information about its most fundamental properties. Using photoelectron imaging spectroscopy and ab initio calculations, we illuminate some of the anion's features, including its photoelectron spectrum and detachment energy, as well as the electron affinity of neutral oxalyl chloride. The spectroscopic results for this anion are compared to the recently reported studies of glyoxal,[10] methylglyoxal,[11] and biacetyl.[12]

2. EXPERIMENTAL METHODS

Caution: Expert care is required in handling oxalyl chloride. Under normal conditions, it is a colorless, sharp-smelling liquid, which is toxic by inhalation. It is also corrosive enough to have once destroyed a jumbo jet airplane.[13]

The experiments were carried out using a negative-ion photoelectron[14] imaging[15-17] spectrometer described elsewhere.[18] In short, 98% pure oxalyl chloride (Alfa Aesar, Thermo Fisher Scientific, Inc.) was transferred to a sample holder inside a fume hood. The sample holder was then connected to the gas delivery lines feeding the pulsed nozzle inside the ion source chamber. By passing Ar carrier gas at an absolute backing pressure of approximately 3.5 atm over the liquid sample (vapor pressure 0.2 atm at ambient temperature), a ~ 6% mixture of oxalyl chloride vapor and Ar was created. The gas mixture was expanded into the high-vacuum chamber (10^{-7} torr base, 10^{-5} torr operational pressure) through a pulsed supersonic nozzle (General Valve Series 9, Parker, Inc.) operated at a 50 Hz repetition rate matching that of the laser.

The supersonic expansion was bombarded with approximately 70 eV thermionic electrons from a heated thorium-coated iridium ribbon filament placed about a centimeter downstream from the nozzle and at the right angle to the expansion axis. The generated anions continued to drift with the expansion, continuously cooled by collisions with the carrier gas. About 15 cm downstream from the nozzle, they were extracted into a Wiley-McLaren[19] linear time-of-flight mass-

spectrometer. The extraction was accomplished using a metal repeller plate pulsed from the baseline ground potential to approximately –900 V at the approximate time of the arrival of the ions.[20] The anions were further accelerated to approximately 2.5 keV of kinetic energy, steered, focused, and separated according to their mass-to-charge ratios within a 2 m long flight tube, before entering the detection region of the instrument, housing a parent-anion detector and a velocity-map[21] photoelectron imaging[16] assembly.

The ion detector (Burle, Inc.) consists of two 25 mm diameter microchannel plates (MCP) coupled to a metal anode. The time-resolved signal from the detector was fed into an oscilloscope and used to optimize the intensity and the focusing of the parent-ion time-of-flight mass-spectrum. Within the imaging assembly, the anion beam was intersected at 90° with a pulsed (7 ns) linearly polarized light beam from a 50 Hz Spectra Physics, Inc. LAB-130-50 Nd:YAG laser. The experiments described here used 532 and 355 nm radiation obtained as the second and third harmonics of the laser's fundamental output. The electrons photodetached from the mass-126 anions were electrostatically projected by a series of velocity-map electrodes in the direction orthogonal to both the ion and laser beams and detected using a 40 mm diameter position-sensitive dual-microchannel-plate imaging detector coupled to a P43 phosphor screen (Burle, Inc.). Photoelectron impact positions on the detector were recorded by a thermoelectrically cooled CCD camera (CoolSNAP Myo, Photometrics, Inc.).

The reported images correspond to multiple runs, totaling ~10^6 experimental cycles each. The inverse Abel transformation[16] implemented in the BASEX program[22] was used to extract the photoelectron speed and angular distributions. Speed v and the emission angle with respect to the laser polarization direction are the native observables of *velocity*-map imaging. Since chemically relevant information is contained in the energy (rather than speed) spectra, the native speed distribu-

tions $I_0(v)$ were converted to the energy domain using the Jacobian transform $I_0(v)dv = I(\varepsilon)d\varepsilon$, where $\varepsilon = mv^2/2$ is electron kinetic energy (eKE), to yield the conventional photoelectron spectra:

$$I(\varepsilon) = I_0(v)dv/d\varepsilon \propto I_0(v)/v \quad (1)$$

The spectra were calibrated using the well-known electron affinity of atomic oxygen.[23-24] All energy-domain spectra in this work are plotted versus electron binding energy, eBE = $h\nu - \varepsilon$, to allow for direct comparison of the result obtained at different laser wavelengths.

3. GEOMETRIC STRUCTURES

Since little prior information is available about the anion of oxalyl chloride, we begin with the analysis of its geometric structures. After these basic properties are defined, we will turn to the spectroscopic investigation using anion photoelectron imaging, as described in the next Section.

The Lewis structure of the neutral $(COCl)_2$ molecule (Scheme 1) allows for a nearly free internal rotation about the C–C sigma bond with respect to the Cl–C–C–Cl dihedral angle, *d*. The torsional potential is rather flat, but does have a few defined minima.[2] The structure in Scheme 1 (C_{2h} symmetry, $d = 180°$) corresponds to the most stable *anti* conformer. In this work, we clearly delineate the *anti* vs. *trans* and *syn* vs. *cis* structures. Although these terms are sometimes used interchangeably, this practice would lead to a lack of clarity in the present investigation. In short, the *anti*, *gauche*, and *syn* structures correspond to neutral oxalyl chloride, while *trans* and *cis* to the anion. The *anti* conformer in Scheme 1 should not be referred to as a *trans* isomer, because its geometry is not "locked" with respect to internal rotation. Similarly, the alternative planar structure (C_{2v} symmetry, $d = 0°$) corresponds to the *syn* conformer, not *cis* isomer. An intermediate structure of C_2 symmetry ($0° < d < 180°$) corresponds to a *gauche* conformation.

Previous studies in the gas phase revealed the coexistence of the *anti* and *gauche* conformers

of oxalyl chloride, with no contribution from *syn*.[2,25] For the *gauche* conformer, electron diffraction experiments indicated d = 55(6)° or 76(18)°, depending on the study,[25-26] while the *ab initio* values range between d = 87° and 91°, depending on the method.[27-28] It is important for the present work that the majority of neutral oxalyl chloride is found in the *anti* form, but the *gauche* conformer, which is only 0.04 eV less stable, still accounts for a significant mole fraction (~30% at 0 °C).[25-26] The *syn* structure, another 0.05 eV higher than *gauche*,[2] is not a true potential minimum, but a saddle point separating the equivalent *gauche* conformers at $d \approx \pm 90°$.

The anion of oxalyl chloride differs significantly from the neutral, because of the additional half-bond of π character between the carbon atoms. The highest- (singly-) occupied MO (HOMO) of the C_{2h} symmetry anion structure (details to follow) is shown in Figure 1. Its π bonding character with respect to the C–C bond shortens this bond in the anion and locks the structure with respect to internal rotation, resulting in potential minima at d = 180° (C_{2h}) and 0° (C_{2v}). It also precludes the existence of an intermediate ($0° < d < 180°$) minimum on the anion potential. Although the C_{2h} and C_{2v} anion structures look similar to the respective *anti* and *syn* conformations of neutral oxalyl chloride, they cannot easily inter-convert and should therefore be referred to as the *trans* and *cis* *iso*mers, rather than *anti* and *syn confor*mers.

These preliminary considerations are confirmed by the electronic structure calculations using the Q-Chem 5.1 program package.[29] Some of the key results are summarized in Figure 2. The initial geometry optimizations and potential energy scans were performed using the B3LYP density functional with the aug-cc-pVDZ basis set. As expected, a cursory scan of the anion potential with respect to d (relaxed with respect to other coordinates under the C_2 symmetry constraint) indicated a >1 eV barrier separating the *trans* and *cis* forms of $(COCl)_2^-$. The barrier, indicated schematically by the dashed gray curve in Figure 2, is large enough for us not to be concerned

about its exact magnitude. For this reason, higher-level investigations of the *trans* ↔ *cis* interconversion were not pursued.

The *trans* and *cis* anion geometries, as well as the global-minimum neutral structure (*anti*), were optimized using the coupled-cluster theory with single and double excitations (CCSD). Initial CCSD optimizations employed the aug-cc-pVDZ basis set, followed by further optimizations with the aug-cc-pVTZ basis. The final state energies were determined from the single-point calculations including the non-iterative triples corrections, CCSD(T), with the aug-cc-pVTZ basis set. The complete geometric parameters of the CCSD/aug-cc-pVTZ optimized *trans* (C_{2h}) and *cis* (C_{2v}) anion structures are given in Table 1. In Figure 2 and throughout, we refer to these geometries as simply *trans* and *cis*, thus distinguishing them from the respective *anti* and *syn* neutral structures. The optimized parameters of the neutral *anti* conformer are also included in Table 1.

4. EXPERIMENTAL RESULTS

The mass-spectrum of $(COCl)_2^-$ anions consists of a triplet of peaks at 126, 128, and 130 a.m.u. with a characteristic ~9:6:1 intensity ratio due to the approximately 3:1 abundance ratio of the ^{35}Cl and ^{37}Cl isotopes. A sample parent-ion spectrum is shown in Figure 3. The most intense 126 a.m.u. peak was used in the photoelectron imaging experiments.

Before describing the spectroscopic results, it is important to consider the implications of the large torsional barrier on the anion potential in oxalyl chloride (Figure 2). Based on the previous studies,[2,25] we must assume the presence of both *anti* and *gauche* conformers of neutral $(COCl)_2$ in the precursor expansion. It is not clear what temperature should be ascribed to the neutral molecules just before the anion formation. Since it occurs within electron-impact ionized plasma, the process cannot be modeled using the typical supersonic temperature of a few Kelvin. It is reasonable to expect that the *anti* conformer yields predominantly *trans*-$(COCl)_2^-$, while *gauche*

can generate either *trans* and *cis* anions, likely in similar quantities. If we assume a 0.70/0.30 *anti*/*gauche* ratio for the neutral precursor,[25-26] ~0.85 and ~0.15 mole fractions of the *trans* and *cis* anions should be expected. Once the anions are cooled to a typical ion-beam temperature of ~70 K,[20] the torsional barrier makes the *cis* ↔ *trans* interconversion unlikely. In sum, while it is difficult to predict the exact populations, the *trans* isomer is expected to dominate, but some fraction of the anions may be trapped in the *cis* state.

Figure 4 shows the photoelectron images and spectra obtained at 355 and 532 nm. Figure 4a displays both spectra plotted together for comparison. Figures 4b and 4c separate the spectra and compare them to the model simulations described in Section 6. Figures 4b and 4c also include the original photoelectron images from which the spectra were obtained. The right and left halves of the image in Figures 4b correspond to the raw and Abel-inverted data, respectively.

The 355 nm spectrum (Figures 4a and 4b) consists of a single broad band assigned to the electronic transition from the ground state of the anion to the ground state of neutral oxalyl chloride. The width of the band indicates significant difference between the equilibrium geometries of these states. The band maximum at about 2.3 eV corresponds (approximately—see Section 6) to the anion's vertical detachment energy (VDE). The poorly defined onset at approximately 1.8 eV corresponds to the adiabatic electron affinity (EA) of oxalyl chloride. The 532 nm spectrum (Figures 4a and 4c) at first glance looks like the lower-energy part of the 355 nm band, if it were split almost evenly into two halves. However, the sharp onset of the 532 nm spectrum at eBE → $h\nu$, corresponding to low-eKE electrons, is uncharacteristic of regular photodetachment and requires further analysis (Section 6).

The photoelectron angular distributions[30-32] (PAD) with respect to the laser polarization direction were obtained from the photoelectron images using the BASEX program.[22] For the 355

nm data, the PAD was determined by integrating the angle-dependent image intensity over the nearly complete energy range of the band (Figures 4a and 4b), eBE = 1.70 – 2.79 eV. The angular dependence of the 532 nm data was analyzed in the range of eBE = 1.86 – 2.16 eV. The lower bound corresponds to eBE where the band intensity rises more than twofold above the noise level. The upper bound was chosen specifically to exclude the slow-electron signal at the image center, corresponding to the sharp peak at eBE $\rightarrow h\nu$. In Section 6, this threshold spike will be attributed to a different photodetachment mechanism, compared to the rest of the 532 nm image.

The photoelectron anisotropy parameter (β) values determined as described above are plotted in Figure 5 against the corresponding average eKEs. The large horizontal "error bars" for the two data points are neither errors nor uncertainties: they indicate the respective energy intervals over which the PADs were analyzed (see above). The vertical error bars in each case do indeed represent the statistical uncertainties in determining the β values from the experimental data.

5. ELECTRONIC STRUCTURE

5.1. Bound States. The oxalyl chloride anion is obtained by adding an electron to the closed-shell neutral molecule. According to the calculations in Section 3, *trans*-$(COCl)_2^-$ has an $X\,^2A_u$ ground state with the electron configuration $[X\,^1A_g](4a_u)^1$, where $X\,^1A_g$ is the neutral state. The $4a_u$ orbital is shown in Figure 1a and all relevant electron configurations are expanded in Tables 2 and 3. The ground state of the *cis* anion is X^2B_2: $[X\,^1A_1](4b_2)^1$ (Table 3). The B_2 irreducible representation is defined assuming the molecular plane is the primary σ_v mirror plane.

Using the CCSD(T) results in Section 3, the adiabatic EA, the relative energies of the anion isomers, and the vertical attachment and detachment energies can be calculated from the differences, ΔCCSD(T), of the appropriate state energies. These results are included in Tables 2 and 3. Table 2 lists the anion and neutral state energies, each calculated for the C_{2h} *trans* and *anti*

geometries (Table 1). As discussed in Section 3, these are the equilibrium geometries of the anion and neutral, respectively. Therefore, the energy difference between the *anti*-neutral and *trans*-anion structures corresponds to adiabatic EA of the neutral. The differences between the *trans*-neutral states and the *trans*-anion are the VDEs of the anion for transitions to these neutral states. Finally, the difference between the *anti*-neutral and *anti*-anion is the vertical attachment energy (VAE) of the neutral. Table 3 lists the relative state energies at the *cis* geometry only, i.e., all values in the table represent the VDEs for the *cis*-anion transitions to different neutral states.

So determined EA = 1.797 eV (Table 2) for *anti*-oxalyl chloride agrees with the observed onsets of the detachment bands in Figure 4. The VDE of the *trans*-anion, calculated using the ΔCCSD(T) method, is 2.284 eV, matching closely the position of the maxima of the 355 and 532 nm bands in Figure 4. The ΔCCSD(T) results further predict that the ground state of the *cis* anion is 0.126 eV higher in energy than the *trans* minimum (Figure 2) and has a VDE of 2.219 eV.

The ΔCCSD(T) results are in good agreement with the experiment, but they do suffer from the shortcoming of relying on different electronic wave function references to describe the anion and neutral states.[33] The problem is resolved within the equation-of-motion (EOM) approach. To model the photodetachment transitions, we performed single-point EOM-XX-CCSD/aug-cc-pVTZ ionization-potential (XX = IP) and electron-affinity (XX = EA) calculations[33] for the *trans* and *cis* geometries. In the IP calculations, an alpha- or beta-spin electron, as appropriate, was removed from the unrestricted X^2A_u/X^2B_2 (*trans*/*cis*) anion reference, giving access to the ground and lowest-excited states of neutral oxalyl chloride. The EA transitions were analyzed by adding an A_u/B_2 symmetry electron to the closed-shell (restricted) X^1A_g/X^1A_1 neutral reference, yielding the X^2A_u/X^2B_2 states of the anion. The non-iterative triples corrections (fT)[34] were included in the IP transition energies for the *trans* anion. Technical issues prevented us from directly calculating

the fT corrections for the *cis* structure, so the *trans* fT values for the corresponding neutral states were used instead. The results (corresponding to the anion VDEs) are summarized in Tables 2 and 3 for the *trans* and *cis* structures, respectively. Among the different methods, the recommended values are bolded. These quantities were used to construct the energy diagram in Figure 2.

For the lowest-energy photodetachment transition in the dominant *trans* form of the anion, all results in Table 2 are in agreement with the experimental spectra in Figure 4. In Section 6.1, we will show that the highest-level, EOM-IP-CCSD(fT), energy for the $X\,^2A_u \rightarrow X\,^1A_g$ transition, 2.335 eV, matches the VDE = 2.33(4) eV determined from the experiment. These calculations also predict the lowest triplet (^3A_u) and the corresponding open-shell singlet (^1A_u) states of the neutral to lie 5.197 and 5.351 eV (vertically) above the *trans* anion ground state. These transition energies are not accessible with our laser, but taken together with the ground-state VDE, they translate into a 2.862 eV singlet-triplet ($S_0 \rightarrow T_1$) and a 3.016 eV singlet-singlet ($S_0 \rightarrow S_1$) vertical excitation energies for the *trans* anion of oxalyl chloride. These results can be indirectly but favorably compared to the corresponding adiabatic values for *anti* oxalyl chloride determined from the UV/VIS absorption: 3.022 eV ($S_0 \rightarrow T_1$) and 3.371 eV ($S_0 \rightarrow S_1$).[35]

5.2. Anionic Resonances. The intense signal at the eBE $\rightarrow h\nu$ (eKE $\rightarrow$ 0) threshold in the 532 nm spectrum (Figure 4) may be a signature of autodetachment from an excited anionic state (a resonance) embedded in the detachment continuum.[36-37] To investigate this possibility, we carried out several types of EOM-CCSD studies[33] targeting electronically excited states of the oxalyl chloride anion at its dominant *trans* geometry. First, the excitation-energy (EE) methodology, EOM-EE-CCSD/aug-cc-pVTZ, was used to identify the excited states of the anion by means of one-electron spin-conserving excitations from the $X\,^2A_u$ anion reference. Second, the EOM-EA-CCSD calculations, where we add an electron to the $X\,^1A_g$ neutral reference, were extended to

target not only the ground state of the anion (Table 2), but also the excited states. Third, these states were characterized within the non-Hermitian quantum-mechanical framework using a complex absorbing potential (CAP) with the EOM-EA-CCSD method.[38-41] The last approach was necessary, because all electronically excited states of the *trans* anion proved to be unbound resonances, i.e. they lie above the anion's vertical detachment threshold. Similar calculations for the *cis* anion led to the same conclusion.

The details of these calculations for the *trans* anion structure are summarized in the Supporting Information. The main conclusion is that there are indeed low-lying anionic states embedded in the detachment continuum close to the anion VDE and, by coincidence, the 532 nm photon energy. The two lowest excitation transitions give rise to the ^2B_u and ^2A_g resonances, which are indicated schematically in Figure 2. The ^2B_u state is optically "dark", i.e., not accessible from the $X\,^2A_u$ state of the anion via a one-photon electric-dipole transition, while ^2A_g is dipole-allowed and, therefore, "bright". Their energies, calculated using different methods and basis sets, are listed in Table S1.

Specifically, the CAP-EOM calculations place the ^2A_g resonance ~0.3 eV above the neutral and ~2.4 eV above the anion ground state. In comparing the latter to the 2.33 eV energy of 532 nm photons, the resonance width (~0.3 eV) and the unknown Franck-Condon width of the $X^2A_u \rightarrow {}^2A_g$ transition should be kept in mind. Therefore, the ^2A_g resonance is likely to be accessible from the *trans*-anion ground state with 532 nm photons. It may also be vibronically coupled to the dark ^2B_u state or to the dense highly vibrationally excited levels of the X^2A_u state, setting up plausible pathways for vibrationally mediated autodetachment discussed in Section 6.3.

6. SPECTRAL MODELING AND DISCUSSION

6.1. Direct photodetachment. The entire 355 nm spectrum in Figure 4b can be interpreted in terms of a single photodetachment transition from the ground state of the anion to the ground

electronic state of the neutral. The *trans* anion is expected to dominate the spectrum and its predicted VDE = 2.335 eV (Table 2) is in excellent agreement with the 355 nm band properties. Some contribution of the *cis* isomer cannot be excluded, but due to the congested nature of the band and similarity of the *trans* and *cis* VDEs (Tables 2 and 3), the isomers are not resolved.

The 355 nm photodetachment band has an approximately Gaussian shape, peaking near eBE = 2.3 eV. Congested band maxima are commonly associated with the anion's VDE, but the two do not always match. Within the Born-Oppenheimer approximation, the photodetachment cross-section is separable into the electronic and vibrational (Franck-Condon) parts, and it is the vibrational envelope alone that peaks at eBE = VDE. The electronic part generally varies with the photon energy and eKE and can shift the observed band maximum away from the VDE. Such shifts are particularly significant in the low-eKE regime, where the electronic part of the cross-section changes rapidly with eKE due to the Wigner law.[42-43]

In previous studies, we modeled congested bands using the Wigner-scaled Gaussian (WSG) function:[44-47]

$$\mathrm{WSG(eBE)} = \begin{cases} N(h\nu - \mathrm{eBE})^P \exp\left(-\frac{(\mathrm{eBE}-\mathrm{VDE})^2}{2w^2}\right), & \mathrm{eBE} \le h\nu \\ 0, & \mathrm{eBE} > h\nu \end{cases} \quad (2)$$

The Gaussian part of WSG approximates the Franck-Condon envelope peaking at the transition's VDE, while $(h\nu - \mathrm{eBE})^P = \varepsilon^P$ multiplied by the Heaviside function $\Theta(h\nu - \mathrm{eBE})$ is a Wigner pre-factor accounting for the eKE-dependent scaling of the electronic cross-section. With $P = l + 1/2$, the electronic term corresponds to the Wigner threshold law,[42,48] $\sigma \propto \varepsilon^{l+1/2}$, where l is the orbital angular momentum quantum number of the outgoing electron. As an approximation, we will use $l = 0$ ($P = 0.5$), corresponding to *s* partial waves, which are the lowest-order dipole-allowed waves in both the $X^2\mathrm{A}_u \rightarrow X^1\mathrm{A}_g$ and $X^2\mathrm{B}_2 \rightarrow X^1\mathrm{A}_1$ photodetachment transitions in the respective

trans and *cis* anions. Although the final state of the electron is generally a superposition of l-waves, the lowest orders dominate at small eKEs, making the above scaling most appropriate.[45] N in Eq. 2 is a normalization constant and w is a Franck-Condon width parameter.

A fit of Eq. 2 with $P = 0.5$ to the 355 nm spectrum of oxalyl chloride is shown by the dashed line in Figure 4b. Although the experimental spectrum peaks at 2.26(2) eV, the WSG model indicates (as expected) a slightly larger VDE of 2.33(4) eV, with the width parameter $w = 0.29$ eV. The small shift of the apparent maximum from the VDE is due the electronic cross-section scaling described by the Wigner pre-factor in Eq. 2. VDE = 2.33(4) eV matches the 2.335 eV value predicted for the *trans*-anion by EOM-IP-CCSD(fT)/aug-cc-pVTZ (Table 2). It also happens to coincide with the energy of 532 nm photons, making the 532 nm data particularly informative.

If the 355 and 532 nm spectra (Figure 4a) are to be assigned to the same transition, they both should be modeled using the same transition properties. In Eq. 2, VDE is the anion's property independent of the wavelength. The same applies to the Franck-Condon envelope, with a caveat that w reflects a convolution of the transition's native width with the experimental broadening, which does depend on eKE and, therefore, $h\nu$. The experimental resolution is a constant in the measurement's native domain (velocity or speed): i.e., Δv = const (independent of v). Upon the $v \rightarrow \varepsilon$ transformation (Eq. 1), we get $\Delta\varepsilon \propto v\Delta v$ or $\Delta\varepsilon \propto \sqrt{\varepsilon}$, i.e. the experimental broadening increases with increasing eKE. For this reason, the convoluted width parameter w in Eq. 2 is expected to be smaller for the 532 nm spectrum, compared to 355 nm (for the same transition).

For analysis of the 532 nm data, we turn to Figure 6. In each part a-c, the experimental spectrum from Figure 4a is plotted twice: with respect to eBE in the main plot and with respect to speed v (proportional to camera pixels) in the inset. Although the eBE and v spectra are equivalent, the speed domain helps to decompress the slow-electron features.

The first point about Figure 6 is that a lone WSG(P = 0.5) function, representing the same detachment channel as that at 355 nm, cannot describe the low-eKE region of the 532 nm spectrum. At $h\nu \approx$ VDE, Eq. 2 scales as WSG $\propto \varepsilon^{1/2}$ at $\varepsilon \to 0$, while its transform into the speed domain (Eq. 1) behaves as $\propto v^2$ for $v \to 0$. These scalings arise from the Wigner pre-factor and have nothing to do with the Franck-Condon envelope. Our modeling shows that it is impossible to match both the low-eKE onset and the bulk of the 532 nm spectrum using one WSG(P = 0.5) function with the VDE and w parameters that are consistent with the 355 nm values. The WSG curves marked D_1 in Figure 6a,b and D in Figure 6c (D for Direct photodetachment) each assume VDE = 2.33 eV, as determined from the 355 nm data. The w values are reduced from 0.29 eV for 355 nm to 0.22 eV (D_1) or 0.23 eV (D) for 532 nm, to account for the improved resolution at lower eKEs. The only substantive difference between the D_1/D curves in Figure 6 is the value of the normalization coefficient N (Eq. 2). A striking discrepancy between each of these curves and the experimental spectrum is observed in the small-eKE region. The D_1/D model curves cannot match the initial rate of onset in the data with increasing ε or v. To explain this discrepancy, we must assume either a departure from the Wigner law or an additional transition contributing to the 532 nm spectrum, not seen at 355 nm.

6.2. *Cis* dipole effect. Regarding the first possibility, a faster than $\varepsilon^{1/2}$ rise of the slow-electron cross-section may occur, if the long-range interaction between the ejected electron and the remaining neutral molecule is dominated by a charge-dipole potential.[49] While the oxalyl chloride molecule at the *trans* anion geometry has no dipole moment, the *cis* neutral structure has a dipole of 1.70 Debye, per the CCSD/aug-cc-pVTZ calculations in Section 3. To be clear, a non-point dipole of this magnitude is not sufficient to support a dipole-bound anion state,[50] but it can modify the low-eKE behavior of the cross-section. For polar molecules, the WSG definition in Eq. 2 must

allow the Wigner exponent (P) values not limited to half-integers.[49,51-52]

In general, P depends on the dipole magnitude, the electron symmetry, and the rotational states of the anion and the molecule.[49] Since multiple rotational states may contribute to the same partial wave, the Wigner exponent is not a constant for a given photodetachment channel in a polar molecule, but has a range of values. However, the low-eKE process is still dominated by the lowest P magnitude, so in practice we need to focus on the lower bound of the P range. Recently, Wester and co-workers considered how the dipole moment controls the range of P values.[51] They showed that in the photodetachment of rotationally cold NH_2^- (neutral dipole moment 2.04 Debye),[53] the Wigner exponent for the s partial wave ranges from 0.12 to nearly 0.5.[51] For *cis*-$(COCl)_2^-$, the neutral dipole moment is 1.70 Debye and the lowest P value expected under the same assumptions is 0.29 (based on Figure 3 in Ref. 51). Substituting $P = 0.29$ into Eq. 2 with VDE = 2.26 eV (Table 3) and $w = 0.22$ eV (the same as for D_1) yields the WSG curve marked D_2 in Figure 6a.

Putting it together, the red curve $D_1 + D_2$ in Figure 6a represents direct photodetachment of the *trans* and *cis* anions. The normalization constants for D_1 and D_2 are set in proportion to the expected populations, $N_1/N_2 = 0.85/0.15$ (Section 4). Although this ratio is but a guess, no reasonable combination of D_1 and D_2 matches both the low-eKE rise and the bulk of the 532 nm spectrum, regardless of the relative N_1 and N_2 values. To match the experimental spectrum, a faster onset of the model band is required.

Since the cold-anions assumption may not apply, we also considered the extreme case of $P = 0$. This value turns the Wigner pre-factor in Eq. 2 into the Heaviside function $\Theta(h\nu - \mathrm{eBE})$, yielding a step-like rise at $\mathrm{eBE} = h\nu$. The corresponding WSG curve, assuming VDE = 2.26 eV and $w = 0.22$ eV, is marked D_2 in Figure 6b. It must be combined with the contribution of the *trans* anion, D_1, as shown by the $D_1 + D_2$ curve in the figure. As in Figure 6a, $D_1 + D_2$ assumes a 0.85/0.15

trans/cis ratio, but regardless of its exact value, the match of the model band to the experimental spectrum at eBE $\rightarrow h\nu$ is not good.

6.3. Autodetachment. Alternatively, sharp low-eKE features in photoelectron spectra can be attributed to autodetachment (AD) from metastable anionic states (resonances). In Section 5.2, we identified two low-lying anionic resonances of oxalyl chloride. We now hypothesize that one of these resonances, the optically bright ^2A_g state, may account for the low-eKE electrons in the 532 nm spectrum. The proposed mechanism involves photoexcitation of the resonance, followed by its coupling to the highly-excited vibrational levels of the ground electronic state of the anion. These levels are above the global potential minimum of neutral oxalyl chloride and may decay via a statistical process of thermionic emission (TE) of an electron.[54-55] The first step in this mechanism relies on a bright excited anionic state accessible with the laser photons. It may explain the appearance of the AD feature at one wavelength (532 nm), but not the other (355 nm). As shown below, the AD mechanism explains the observed spectral features by invoking only the dominant *trans* isomer of the anion, with a minor contribution of the *cis* isomer assumed to be hidden underneath.

The TE model was originally developed for clusters with large numbers of coupled degrees of freedom,[56-59] but its application was also demonstrated for molecular dimer anions of carbonyl sulfide,[45] which are similar in size to oxalyl chloride. The model assumes that following the absorption of a photon the available energy is partitioned among all vibrational modes. The statistical distribution of the emitted electrons is given by the Klots formula:[56,60]

$$P_{AD}(\varepsilon) = N\varepsilon^{1/2}\exp\left(-\varepsilon/k_B T_{TE}\right) \tag{3}$$

which is easily converted to eBE via $\varepsilon = h\nu - \mathrm{eBE}$:

$$P_{AD}(\mathrm{eBE}) = N(h\nu - \mathrm{eBE})^{1/2}\exp\left(-(h\nu - \mathrm{eBE})/k_B T_{TE}\right), \quad \mathrm{eBE} \le h\nu \tag{4}$$

Eq. 4 is reminiscent of Eq. 2 with $P = 0.5$. As before, $\varepsilon^{1/2}$ is the Wigner pre-factor for *s* partial

waves, while the Boltzmann exponent replaces the Gaussian Franck-Condon envelope. The characteristic temperature T_{TE} is the microcanonical temperature of the remaining neutral species. It intuitively relates to the initial temperature of the anions T_0 and the excitation energy $h\nu$, corrected for the cost of removing an electron, i.e. the adiabatic EA:[54-55,57]

$$T_{TE} = T_0 + (h\nu - \mathrm{EA})/C_v \tag{5}$$

The heat capacity in Eq. 5 is the microcanonical quantity $C_v = (3n-7)k_B$,[54-56] determined by the coupling of a given vibrational mode with the $(3n-7)$ other oscillators (n is the number of atoms, $n = 6$). Since not all modes may be equally active, an effective number of oscillators may be used, but we found no need to deviate from $C_v = 11k_B$ prescribed by the fully statistical model. Previously, we arrived at the same conclusion for the autodetachment in $(OCS)_2^-$.[45]

Assuming EA = 1.797 eV (Table 2) and T_0 ~ 70 K (a typical anion beam temperature),[20] the characteristic temperature for the AD process at 532 nm is T_{TE} ~ 630 K (Eq. 5). Substituting this into Eq. 4 yields the model curve marked AD in Figure 6c. This curve shows a much faster onset than the direct photodetachment curve D. Combined with D (Eq. 2 with $P = 0.5$), the overall D + AD model yields a very good agreement with the experimental spectrum, something that no combinations of direct photodetachment curves in Figure 6a,b could achieve. Only the relative values of the normalization coefficients were treated as adjustable parameters in Figure 6c.

The D + AD curve from Figure 6c is reproduced in Figure 4c, which also shows the residual (gray), calculated by subtracting (D + AD) from the experimental spectrum. The residual reveals what was omitted from the D + AD simulation: the partial details of a vibrational structure in the experimental spectrum. The progression of residual peaks spaced by 1020(40) cm^{-1} is in excellent agreement with the 1028 cm^{-1} harmonic frequency (B3LYP/aug-cc-pVTZ) of an in-plane a_g symmetry mode of neutral oxalyl chloride. The atomic motions involved in this mode are illustrated

in the inset in Figure 4c. They include primarily the C-C and C-Cl stretches and the C-C-O bend—notably, the same geometric parameters that show the greatest changes from the anion (*trans*) to neutral (*anti*) equilibria (Table 1). The nearest other vibrational frequencies, predicted by the calculations, are 738 and 1838 cm^{-1}, making the observed match even more compelling.

6.4. Photoelectron Angular Distributions. The PADs give insight into the electronic structures, in particular the orbitals from which the emitted electrons originate.[30-32,61-64] The dominant transition in this work nominally corresponds to electron removal from the $4a_u$ HOMO of the *trans* anion of oxalyl chloride. This Hartree-Fock orbital is depicted in Figure 1a. While it is a good start for describing the PADs, the HOMO is not the only MO participating in the transition. The removal of the canonical HOMO electron affects all electrons in the molecule (as a basic example, the 1*s* orbital in the H atom is not the same as 1*s* in H^-). Although the detachment of a single electron is not a one-electron process, it is possible to describe it as such by using the corresponding Dyson orbital instead of the canonical MO. The Dyson orbital is defined as the overlap between the anion and neutral many-electron wave functions; it thus encodes the changes to all MOs upon the anion → neutral transition.[64] The Dyson orbital for $X^2A_u \rightarrow X^1A_g$ photodetachment of oxalyl chloride, obtained as part of the EOM-IP-CCSD calculations Section 5, is shown in Figure 1b. By inspection, only minor differences between the canonical and Dyson orbitals can be seen. These differences, however, do affect the quantitative modeling of the PADs.

In Figure 5, we compare the experimental β values, determined in Section 4, to the predictions of the ezDyson program by Gozem and Krylov.[65-66] Both the HF and Dyson orbitals shown in Figures 1a,b were imported into ezDyson and the eKE-dependent photoelectron anisotropy values were calculated for each MO by expanding the continuum state of the electron in partial waves up to $l = 6$. Figure 5 shows the resulting $\beta(\varepsilon)$ curves. The overall agreement between the model and

the experiment is quite good. The slightly better apparent agreement of the HF curve with the 355 nm data point should not be over-interpreted: the Dyson orbital is a rigorously more accurate approach to modeling the PADs.[64]

6.5. Comparison to other anions in the glyoxal family. Figure 7 compares the published anion photoelectron spectra of biacetyl (532 nm),[12] methylglyoxal (612 nm),[11] and glyoxal (532 nm)[10] to the new results for oxalyl chloride (355 nm). Each spectrum consists of a single band due to the photodetachment of from the ground state of the anion to the ground state of the neutral.

The electron affinities and detachment energies follow the trend: Biacetyl < Methylglyoxal < Glyoxal << Oxalyl Chloride. Specifically, the anion VDEs are 1.12(5) eV for biacetyl, 1.20(4) eV for methylglyoxal, 1.30(4) eV for glyoxal, and 2.33(4) eV for oxalyl chloride. Each of these molecules is obtained by the substitutions indicated in Figure 7, with glyoxal being the original member of the series. The electron donating property of methyl has a destabilizing effect on the anion, progressively reducing the electron affinity from unsubstituted glyoxal to singly substituted methylglyoxal, and to doubly substituted biacetyl. In contrast, the strong electron-withdrawing (inductive) power of two very electronegative chlorine substituents in oxalyl chloride lends significant stabilization to the anion, resulting in a large (~1 eV) increase in the detachment energy.

7. SUMMARY

We have reported a combined experimental and theoretical investigation into the structure and spectroscopy of the anion of oxalyl chloride. The photoelectron spectra and angular distributions obtained at 355 nm and 532 nm are interpreted in terms of a transition from the ground state of the anion to the ground state of the neutral. The band's onset at ~1.8 eV corresponds to the previously unknown adiabatic EA of oxalyl chloride and is in good agreement with the theory prediction of EA = 1.797 eV. The observed VDE of the anion, 2.33(4) eV, is also in excellent agreement with

the corresponding theory predictions. The 532 nm photoelectron spectrum additionally reveals an uncharacteristically sharp onset near the photon-energy limit, assigned to autodetachment via a low-energy anionic resonance in oxalyl chloride.

These results should be viewed in the broader context of the organic substitution series, which includes glyoxal, methylglyoxal, biacetyl, and oxalyl chloride. The electron affinities and anion detachment energies in this series follow the trend: Biacetyl < Methylglyoxal < Glyoxal << Oxalyl Chloride, which confirms the known properties of the substituents. Specifically, the electron donating character of CH_3 imparts a progressively destabilizing effect on the methylglyoxal and biacetyl anions (singly- and doubly-substituted, respectively). In contrast, the strong electron-withdrawing (inductive) character of Cl strongly stabilizes the anion of oxalyl chloride, resulting in a large increase in its detachment energy, compared to unsubstituted glyoxal.

ASSOCIATED CONTENT

Supporting Information

The Supporting Information is available free of charge at https://xxxxxxx.

Anionic Resonances in Oxalyl Chloride. Table S1: Properties of oxalyl chloride's ^2A_g and ^2B_u anionic resonances at the *trans* geometry. (PDF)

AUTHOR INFORMATION

Corresponding Author

*Email: sanov@arizona.edu

ORCID

Andrei Sanov: 0000-0002-2373-4387

Author Contributions

The manuscript was written through contributions of all authors. All authors have given approval to the final version of the manuscript.

Funding Sources

U.S. National Science Foundation Grant CHE-1664732.

Notes

The authors declare no competing financial interest.

ACKNOWLEDGMENT

The authors thank Professor Robin Polt for his assistance with the safe handling of the toxic and corrosive compound of oxalyl chloride. Financial support of this work was provided by the U.S. National Science Foundation through grant CHE-1664732.

REFERENCES

1. Mohammadkhani, L.; Heravi, M. M., Oxalyl Chloride: A Versatile Reagent in Organic Transformations. *ChemistrySelect* **2019,** *4*, 6309-6337.
2. Chu, G.; Chen, J.; Liu, F.; Shan, X.; Han, J.; Sheng, L., Conformation-specific dissociative photoionization of oxalyl chloride in the gas phase. *Chem. Phys.* **2013,** *416*, 26-32.
3. Holland, D. M. P.; Nandi, S.; Nicolas, C.; Bozek, J. D.; Patanen, M.; Powis, I., An experimental and theoretical study of the valence shell photoelectron spectrum of oxalyl chloride. *Chem. Phys.* **2021,** *542*, 111050.
4. Frost, D. C.; McDowell, C. A.; Pouzard, G.; Westwood, N. P. C., The photoelectron spectra of the oxalyl halides $(COX)_2$, [X = F, Cl and Br]. *J. Electron Spectrosc. Relat. Phenom.* **1977,** *10*, 273-292.
5. Meeks, J. L.; McGlynn, S. P., Photoelectron Spectra of Carbonyls. Oxalyl Chloride, Ethyl Oxalyl Choride, Ethyl Oxamate and N,N-Dimethyl Ethyl Oxamate. *Spectrosc. Lett.* **1975,** *8*, 439-447.
6. Saksena, B. D.; Kagarise, R. E., Rotational Isomerism in Oxalyl Chloride (ClOC–COCl). *J. Chem. Phys.* **1951,** *19*, 987-993.
7. Saksena, B. D.; Jauhri, G. S., Interpretation of the Ultraviolet Spectrum of Oxalyl Chloride. *J. Chem. Phys.* **1962,** *36*, 2233-2235.
8. Baklanov, A. V.; Krasnoperov, L. N., Oxalyl ChlorideA Clean Source of Chlorine Atoms for Kinetic Studies. *J. Phys. Chem. A* **2001,** *105*, 97-103.
9. Ahmed, M.; Blunt, D.; Chen, D.; Suits, A. G., UV photodissociation of oxalyl chloride yields four fragments from one photon absorption. *J. Chem. Phys.* **1997,** *106*, 7617-7624.
10. Xue, T.; Dixon, A. R.; Sanov, A., Anion photoelectron imaging spectroscopy of glyoxal. *Chem. Phys. Lett.* **2016,** *660*, 205-208.
11. Dauletyarov, Y.; Dixon, A. R.; Wallace, A. A.; Sanov, A., Electron affinity and excited states of methylglyoxal. *J. Chem. Phys.* **2017,** *147*, 013934.
12. Dauletyarov, Y.; Wallace, A. A.; Blackstone, C. C.; Sanov, A., Photoelectron Spectroscopy of Biacetyl and Its Cluster Anions. *J. Phys. Chem. A* **2019,** *123*, 4158-4167.
13. Firm told to pay $65 mln for ruining plane *Reuters* [Online], Dec 6, 2007. https://www.reuters.com/article/oddlyEnoughNews/idUSN0620441720071206 (accessed Apr 30, 2021).
14. Ervin, K. M.; Lineberger, W. C., Photoelectron Spectroscopy of Negative Ions. In *Advances in Gas Phase Ion Chemistry*, Adams, N. G.; Babcock, L. M., Eds. JAI Press: Greenwich, 1992; Vol. 1, pp 121-166.
15. Chandler, D. W.; Houston, P. L., Two-Dimensional Imaging of State-Selected Photodissociation Products Detected by Multiphoton Ionization. *J. Chem. Phys.* **1987,** *87*, 1445-1447.
16. Heck, A. J. R.; Chandler, D. W., Imaging Techniques For the Study of Chemical Reaction Dynamics. *Annu. Rev. Phys. Chem.* **1995,** *46*, 335-372.
17. Houston, P. L., Snapshots of Chemistry: Product Imaging of Molecular Reactions. *Acc. Chem. Res.* **1995,** *28*, 453-460.
18. Velarde, L.; Habteyes, T.; Sanov, A., Photodetachment and photofragmentation pathways in the $[(CO_2)_2(H_2O)_m]^-$ cluster anions. *J. Chem. Phys.* **2006,** *125*, 114303.
19. Wiley, W. C.; McLaren, I. H., Time-of-Flight Mass Spectrometer with Improved Resolution. *Rev. Sci. Instrum.* **1955,** *26*, 1150.

20. Johnson, M. A.; Lineberger, W. C., Pulsed Methods for Cluster Ion Spectroscopy. In *Techniques for the Study of Ion Molecule Reactions*, Farrar, J. M.; Saunders, W. H., Eds. Wiley: New York, 1988; pp 591-635.
21. Eppink, A. T. J. B.; Parker, D. H., Velocity map imaging of ions and electrons using electrostatic lenses: Application in photoelectron and photofragment ion imaging of molecular oxygen. *Rev. Sci. Instrum.* **1997,** *68*, 3477-3484.
22. Dribinski, V.; Ossadtchi, A.; Mandelshtam, V. A.; Reisler, H., Reconstruction of abel-transformable images: The Gaussian basis-set expansion abel transform method. *Rev. Sci. Instrum.* **2002,** *73*, 2634-2642.
23. Neumark, D. M.; Lykke, K. R.; Andersen, T.; Lineberger, W. C., Laser Photodetachment Measurement of the Electron-Affinity of Atomic Oxygen. *Phys. Rev. A* **1985,** *32*, 1890-1892.
24. Cavanagh, S. J.; Gibson, S. T.; Gale, M. N.; Dedman, C. J.; Roberts, E. H.; Lewis, B. R., High-resolution velocity-map-imaging photoelectron spectroscopy of the O^- photodetachment fine-structure transitions. *Phys. Rev. A* **2007,** *76*, 052708.
25. Danielson, D. D.; Hedberg, L.; Hedberg, K.; Hagen, K.; Trtteberg, M., Conformational Analysis. 21. The Torsional Problem in Oxalyl Chloride. An ab Initio and Electron Diffraction Investigation of the Structures of the Conformers and Their Energy and Entropy Differences. *J. Phys. Chem.* **1995,** *99*, 9374-9379.
26. Hagen, K.; Hedberg, K., Conformational analysis. I. Molecular structure, composition, trans-gauche energy and entropy differences, and potential hindering internal rotation of gaseous oxalyl chloride as determined by electron diffraction. *J. Am. Chem. Soc.* **1973,** *95*, 1003-1009.
27. Chung, G.; Kwon, Y., Molecular structures of gauche and trans conformers for oxalyl chloride: ab initio and DFT calculations. *J. Mol. Struct.* **2000,** *496*, 199-206.
28. Bokarev, S. I.; Pupyshev, V. I.; Godunov, I. A., Vibronic spectra, ab initio calculations, and structures of conformationally non-rigid molecules of oxalyl halides in the ground and lowest excited electronic states. Part II: Theoretical investigation of oxalyl chloride. *J. Mol. Spectrosc.* **2009,** *256*, 247-255.
29. Shao, Y. H.; Gan, Z. T.; Epifanovsky, E.; Gilbert, A. T. B.; Wormit, M.; Kussmann, J.; Lange, A. W.; Behn, A.; Deng, J.; Feng, X. T., et al., Advances in molecular quantum chemistry contained in the Q-Chem 4 program package. *Mol. Phys.* **2015,** *113*, 184-215.
30. Cooper, J.; Zare, R. N., Photoelectron angular distributions. In *Atomic collision processes*, Geltman, S.; Mahanthappa, K. T.; Brittin, W. E., Eds. Gordon and Breach, Science Publishers: New York, London, Paris, 1968; Vol. XI-C, pp 317-337.
31. Reid, K. L., Photoelectron angular distributions. *Annu. Rev. Phys. Chem.* **2003,** *54*, 397-424.
32. Sanov, A., Laboratory-Frame Photoelectron Angular Distributions in Anion Photodetachment: Insight into Electronic Structure and Intermolecular Interactions. *Annu. Rev. Phys. Chem.* **2014,** *65*, 341-363.
33. Krylov, A. I., Equation-of-motion coupled-cluster methods for open-shell and electronically excited species: The Hitchhiker's guide to Fock space. *Annu. Rev. Phys. Chem.* **2008,** *59*, 433-462.
34. Manohar, P. U.; Krylov, A. I., A noniterative perturbative triples correction for the spin-flipping and spin-conserving equation-of-motion coupled-cluster methods with single and double substitutions. *J. Chem. Phys.* **2008,** *129*, 194105.

35. Godunov, I. A.; Yakovlev, N. N.; Bokarev, S. I.; Abramenkov, A. V.; Maslov, D. V., Vibronic spectra, ab initio calculations, and structures of conformationally non-rigid molecules of oxalyl halides in the ground and lowest excited electronic states. Part I: Reanalysis of the 3680Å and 4100Å absorption systems of oxalyl chloride. *J. Mol. Spectrosc.* **2009,** *255*, 39-44.
36. Moiseyev, N., *Non-Hermitian Quantum Mechanics*. Cambridge University Press: Cambridge, 2011.
37. Klaiman, S.; Gilary, I., On Resonance: A First Glance into the Behavior of Unstable States. In *Adv. Quantum Chem.*, Nicolaides, C. A.; Brändas, E.; Sabin, J. R., Eds. Academic Press: Cambridge, 2012; Vol. 63, pp 1-31.
38. Reisler, H.; Krylov, A. I., Interacting Rydberg and valence states in radicals and molecules: experimental and theoretical studies. *Int. Rev. Phys. Chem.* **2009,** *28*, 267-308.
39. Sneskov, K.; Christiansen, O., Excited state coupled cluster methods. *Wiley Interdiscip. Rev.: Comput. Mol. Sci.* **2012,** *2*, 566-584.
40. Zuev, D.; Jagau, T.-C.; Bravaya, K. B.; Epifanovsky, E.; Shao, Y.; Sundstrom, E.; Head-Gordon, M.; Krylov, A. I., Complex absorbing potentials within EOM-CC family of methods: Theory, implementation, and benchmarks. *J. Chem. Phys.* **2014,** *141*, 024102.
41. Jagau, T.-C.; Zuev, D.; Bravaya, K. B.; Epifanovsky, E.; Krylov, A. I., A Fresh Look at Resonances and Complex Absorbing Potentials: Density Matrix-Based Approach. *J. Phys. Chem. Lett.* **2014,** *5*, 310-315.
42. Wigner, E. P., On the behavior of cross sections near thresholds. *Phys. Rev.* **1948,** *73*, 1002-1009.
43. Lineberger, W. C.; Hotop, H.; Patterson, T. A., Photodetachment Threshold Processes. In *Electron and Photon Interactions with Atoms*, Kleinpoppen, H.; McDowell, M. R. C., Eds. Plenum Publishing Corporation: New York, 1976; pp 125-132.
44. Khuseynov, D.; Dixon, A. R.; Goebbert, D. J.; Sanov, A., Heterogeneous Substitution Effects in Chlorocyanomethyl Radical and Chlorocyanocarbene. *J. Phys. Chem. A* **2013,** *117*, 10681–10691.
45. Surber, E.; Sanov, A., Imaging of Direct Photodetachment and Autodetachment of $(OCS)_2^-$: Excited-State Dynamics of the Covalent Dimer Anion. *Phys. Rev. Lett.* **2003,** *90*, 093001.
46. Wallace, A. A.; Dauletyarov, Y.; Sanov, A., Deprotonation of Isoxazole: A Photoelectron Imaging Study. *J. Phys. Chem. A* **2020,** *124*, 7768-7775.
47. Wallace, A. A.; Dauletyarov, Y.; Sanov, A., Diradical Interactions in Ring-Open Isoxazole. *J. Phys. Chem. A* **2021,** *125*, 317-326.
48. Sadeghpour, H. R.; Bohn, J. L.; Cavagnero, M. J.; Esry, B. D.; Fabrikant, I. I.; Macek, J. H.; Rau, A. R. P., Collisions near threshold in atomic and molecular physics. *J. Phys. B* **2000,** *33*, R93-R140.
49. Engelking, P. C., Strong electron-dipole coupling in photodetachment of molecular negative ions: Anomalous rotational thresholds. *Phys. Rev. A* **1982,** *26*, 740-745.
50. Simons, J., Molecular Anions. *J. Phys. Chem. A* **2008,** *112*, 6401-6511.
51. Lakhmanskaya, O.; Simpson, M.; Murauer, S.; Kokoouline, V.; Wester, R., Photodetachment spectroscopy of cold trapped NH_2^- near threshold. *J. Chem. Phys.* **2018,** *149*, 104302.
52. Simpson, M.; Nötzold, M.; Schmidt-May, A.; Michaelsen, T.; Bastian, B.; Meyer, J.; Wild, R.; Gianturco, F. A.; Milovanović, M.; Kokoouline, V., et al., Threshold photodetachment spectroscopy of the astrochemical anion CN^-. *J. Chem. Phys.* **2020,** *153*, 184309.

53. Bharadvaja, A.; Kaur, S.; Baluja, K. L., Low-energy electron impact cross-sections and rate constants of $$\hbox {NH}_2$$. *Pramana* **2017,** *89*, 30.
54. Andersen, J. U.; Bonderup, E.; Hansen, K., On the concept of temperature for a small isolated system. *J. Chem. Phys.* **2001,** *114*, 6518-6525.
55. Andersen, J. U.; Bonderup, E.; Hansen, K., Thermionic emission from clusters. *J. Phys. B* **2002,** *35*, R1-R30.
56. Baguenard, B.; Pinaré, J. C.; Bordas, C.; Broyer, M., Photoelectron imaging spectroscopy of small tungsten clusters: Direct observation of thermionic emission. *Phys. Rev. A* **2001,** *63*, 023204.
57. Baguenard, B.; Pinaré, J. C.; Lépine, F.; Bordas, C.; Broyer, M., Thermionic emission in small carbon cluster anions. *Chem. Phys. Lett.* **2002,** *352*, 147-153.
58. Surber, E.; Sanov, A., Photoelectron imaging of carbonyl sulfide cluster anions: Isomer coexistence and competition of excited-state decay mechanisms. *J. Chem. Phys.* **2003,** *118*, 9192-9200.
59. Wurz, P.; Lykke, K. R., Multiphoton Excitation, Dissociation, and Ionization of C-60. *J. Phys. Chem.* **1992,** *96*, 10129-10139.
60. Klots, C. E., Unimolecular reactions in a spherically symmetric potential. II. Some tractable potentials. *J. Chem. Phys.* **1994,** *100*, 1035-9.
61. Seideman, T., Time-resolved photoelectron angular distributions: A nonperturbative theory. *J. Chem. Phys.* **1997,** *107*, 7859-7868.
62. Oana, C. M.; Krylov, A. I., Cross sections and photoelectron angular distributions in photodetachment from negative ions using equation-of-motion coupled-cluster Dyson orbitals. *J. Chem. Phys.* **2009,** *131*, 124114.
63. Mabbs, R.; Grumbling, E. R.; Pichugin, K.; Sanov, A., Photoelectron imaging: an experimental window into electronic structure. *Chem. Soc. Rev.* **2009,** *38*, 2169-2177.
64. Krylov, A. I., From orbitals to observables and back. *J. Chem. Phys.* **2020,** *153*, 080901.
65. Gozem, S.; Krylov, A. I., The ezSpectra suite: An easy-to-use toolkit for spectroscopy modeling. *Wiley Interdiscip. Rev.: Comput. Mol. Sci.* **2021**, e1546.
66. Gozem, S.; Gunina, A. O.; Ichino, T.; Osborn, D. L.; Stanton, J. F.; Krylov, A. I., Photoelectron Wave Function in Photoionization: Plane Wave or Coulomb Wave? *J. Phys. Chem. Lett.* **2015,** *6*, 4532-4540.

Table 1. Geometric parameters of the *anti* (C_{2h} symmetry), *trans* (C_{2h}), and *cis* (C_{2v}) structures of oxalyl chloride. The *trans* and *cis* structures correspond to anion equilibria, while the *anti* is the global-minimum geometry of the neutral molecule. All structures were optimized at the CCSD level of theory with the aug-cc-pVTZ basis set. The bond lengths are given in Angstroms, bond angles in degrees.

	anti	*trans*	*cis*
C–C	1.549	1.423	1.430
C–O	1.182	1.219	1.221
C–Cl	1.746	1.844	1.837
∠C-C-Cl	112.2°	110.2°	117.2°
∠C-C-O	123.9°	131.8°	125.8°

Table 2. Nominal electron configurations and relative energies of the ground electronic state of oxalyl chloride anion and several lowest electronic states of neutral oxalyl chloride at C_{2h} *trans* and *anti* geometries, as indicated.

Nominal electron configuration State character	Geometry [a]	Method [b]	Relative energy [c]
Oxalyl chloride anion			
$X\,^2A_u$: …$(13a_g)^2(3b_g)^2(3a_u)^2(12b_u)^2(4a_u)^1$ Anion ground state	*trans*		0
	anti	ΔCCSD ΔCCSD(T)	0.565 **0.598**
Oxalyl chloride (neutral)			
$X\,^1A_g$: …$(13a_g)^2(3b_g)^2(3a_u)^2(12b_u)^2$ Closed-shell singlet	*anti*	ΔCCSD ΔCCSD(T)	1.755 **1.797**
	trans	ΔCCSD ΔCCSD(T) EA-CCSD IP-CCSD IP-CCSD(fT) VDE (exper)	2.340 2.284 2.267 2.414 **2.335** 2.33(4)
$a\,^3A_u$: …$(12a_g)^2(3b_g)^2(3a_u)^2(12b_u)^2(13a_g)^{\uparrow}(4a_u)^{\uparrow}$ Lowest triplet	*trans*	IP-CCSD IP-CCSD(fT) EA-CCSD	5.259 **5.197** 5.133
$A\,^1A_u$: …$(12a_g)^2(3b_g)^2(3a_u)^2(12b_u)^2(13a_g)^{\downarrow}(4a_u)^{\uparrow}$ Open-shell singlet	*trans*	IP-CCSD IP-CCSD(fT)	5.443 **5.351**

[a] The *trans* and *anti* structures correspond to the respective anion and neutral geometries optimized at the CCSD/aug-cc-pVTZ level. Their geometric details are summarized in Table 1.

[b] All calculations in this table were carried out with the aug-cc-pVTZ basis set. The ΔCCSD and ΔCCSD(T) results were obtained as differences between the absolute CCSD or CCSD(T)

energies of the target state and the *trans*-anion ground state, determined in separate calculations. Zero-point vibrational energy corrections are not included. Single-point EOM-XX-CCSD (XX = IP, EA) calculations, abbreviated as XX-CCSD, with or without fT corrections, were carried for the *trans* geometry. The IP calculations were carried out by removing an alpha- or beta-spin electron, as appropriate, from the unrestricted $X\,^2A_u$ anion reference. The EA transitions were analyzed by adding an electron to either the closed-shell (restricted) $X\,^1A_g$ or the unrestricted $a\,^3A_u$ neutral reference, as appropriate. The VDE (exper) value is determined from the model fits to the experimental photoelectron bands shown in Figure 1, as described in Section 5.

[c] Energy values are given in electron-volts, relative to the *trans*-anion ground state. Recommended theory values are in bold.

Table 3. Nominal electron configurations and relative energies of the ground electronic state of the oxalyl chloride anion and several lowest electronic states of the neutral at the *cis* geometry.

Nominal electron configuration State character	Method [a]	Relative energy [b]
Oxalyl chloride anion (*cis*)		
$X\,^2B_2$: …$(13a_1)^2(3a_2)^2(12b_1)^2(3b_2)^2(4b_2)^1$ Anion ground state		0
Oxalyl chloride (neutral)		
$X\,^1A_1$: …$(13a_1)^2(3a_2)^2(12b_1)^2(3b_2)^2$ Closed-shell singlet	ΔCCSD ΔCCSD(T) EA-CCSD IP-CCSD IP-CCSD(fT)	2.264 2.219 2.197 2.340 **2.261**
$a\,^3B_2$: …$(12a_1)^2(3a_2)^2(12b_1)^2(3b_2)^2(13a_1)^{\uparrow}(4b_2)^{\uparrow}$ Lowest triplet	IP-CCSD IP-CCSD(fT)	5.491 **5.429**
$A\,^1B_2$: …$(12a_1)^2(3a_2)^2(12b_1)^2(3b_2)^2(13a_1)^{\downarrow}(4b_2)^{\uparrow}$ Open-shell singlet	IP-CCSD IP-CCSD(fT)	5.663 **5.571**

[a] All calculations were carried out with the aug-cc-pVTZ basis set. The ΔCCSD and ΔCCSD(T) results were obtained as differences between the absolute CCSD or CCSD(T) energies of the target state and the *cis*-anion ground state, determined in separate calculations. Zero-point vibrational energy corrections are not included. Single-point EOM-XX-CCSD (XX = IP, EA) calculations, abbreviated as XX-CCSD, with or without fT corrections, were carried for the *cis* anion geometry (Table 1). The IP calculations were carried out by removing an alpha- or beta-spin electron, as appropriate, from the unrestricted $X\,^2B_2$ anion reference. The EA transitions were analyzed by adding an electron to the closed-shell (restricted) $X\,^1A_1$ neutral reference. The fT corrections from the *trans* calculations (Table 2) are used here.

[b] Energy values are in electron-volts, relative to the *cis*-anion ground state. Recommended values are in bold.

Figure 1

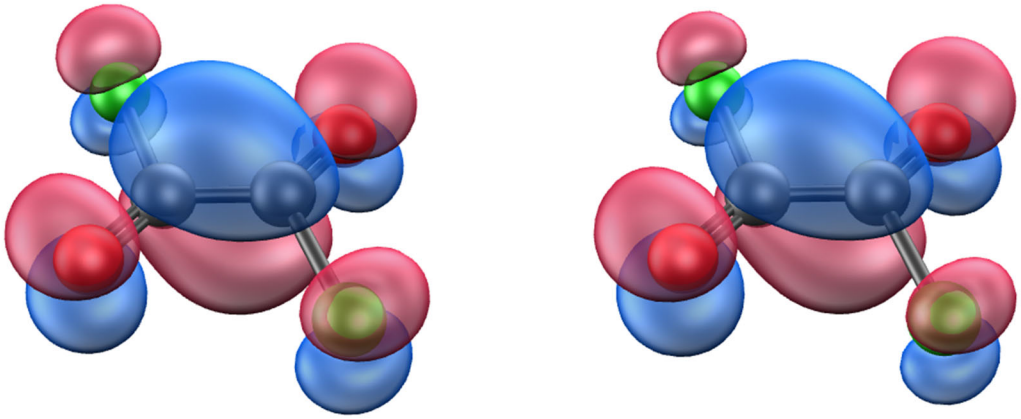

Figure 1. (a) The Hartree-Fock $4a_u$ HOMO of the oxalyl chloride anion (*trans* structure). (b) The Dyson orbital for the $X^2A_u \rightarrow X^1A_g$ photodetachment transition, nominally $(4a_u)^{-1}$, calculated using the EOM-IP-CCSD method (shown is the "left" Dyson orbital). Both orbitals are represented by the 0.04 a.u. isosurface plots and were calculated using the aug-cc-pVTZ basis set.

Figure 2

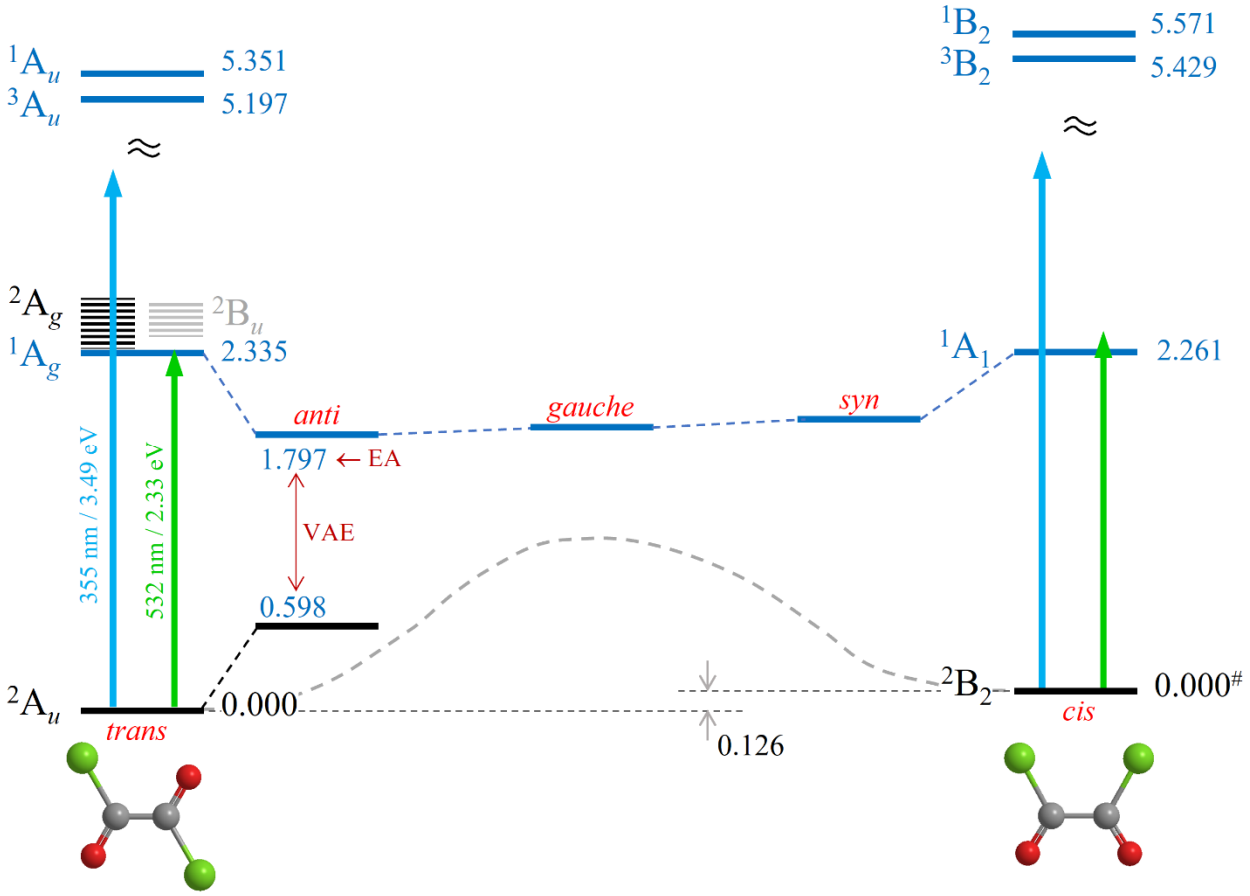

Figure 2. Energy diagram summarizing the results of the calculations reported in Sections 3 and 5. All energy values are in electron-volts. The values on the left (*trans/anti*) side are relative to the *trans* anion structure. The values on the right (*cis*) are reported relative to the *cis* anion (#). See the text for details. All neutral state energies at the *trans* and *cis* anion geometries correspond to the VDEs. The *anti* neutral state energy, relative to the *trans* anion equilibrium, is the adiabatic EA. The difference between the neutral and anion energies at the *anti* neutral geometry (indicated by the double-sided arrow) is the vertical attachment energy (VAE).

Figure 3

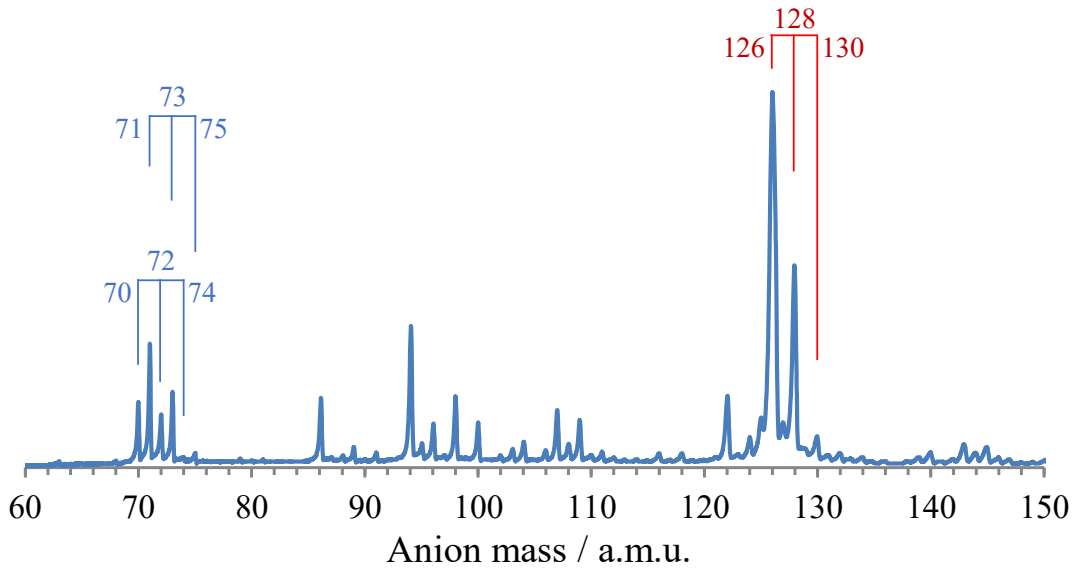

Figure 3. Representative parent anion mass-spectrum. Three-pronged combs indicate mass-triplets corresponding to ions with two chlorine atoms. The oxalyl chloride, $(COCl_2)^-$, triplet is m/z = 126-128-130. m/z = 70-72-74 corresponds to Cl_2^-. m/z = 71-73-75 to HCl_2^-. Tentative assignments of some other peaks (not marked in the figure): m/z = 94-96-98 is $(CCl)_2^-$; m/z = 98-100-102 is the anion of phosgene, $COCl_2^-$.

Figure 4

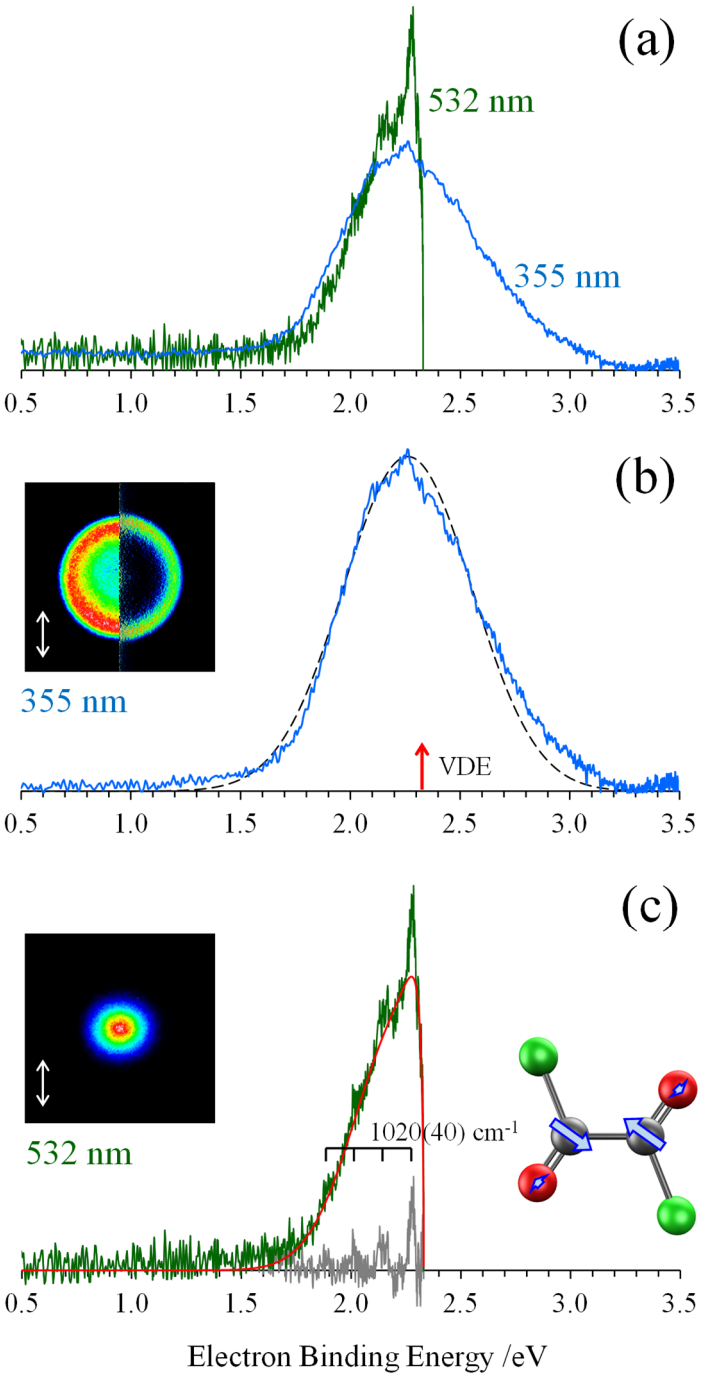

Figure 4. Anion photoelectron images and spectra of oxalyl chloride. (a) Overlaid 355 nm (blue) and 532 nm (green) spectra. Relative normalization is arbitrary. (b) The 355 nm photoelectron

image, with the right and left halves corresponding to the raw and Abel inverted data, respectively. The vertical double arrow indicates the laser polarization direction. The 355 nm experimental spectrum (blue) is overlaid with the model simulation (black dashes) using a single WSG function (Eq. 2), as described in Section 6.1. The red vertical arrow indicates the VDE = 2.33(4) eV value determined from the WSG modeling of the experimental spectrum. (c) The raw 532 nm photoelectron image and the corresponding experimental spectrum (green) overlaid with the model simulation (red) using a combination of the WSG (Eq. 2) and AD (Eq. 4) functions, described in Section 6.3. The gray trace at the bottom is the residual calculated by subtracting the red model curve from the green experimental spectrum. The inset illustrates the atomic motions involved in the vibrational mode assigned to the evenly spaced 1020(40) cm^{-1} progression of peaks seen in the residual.

Figure 5

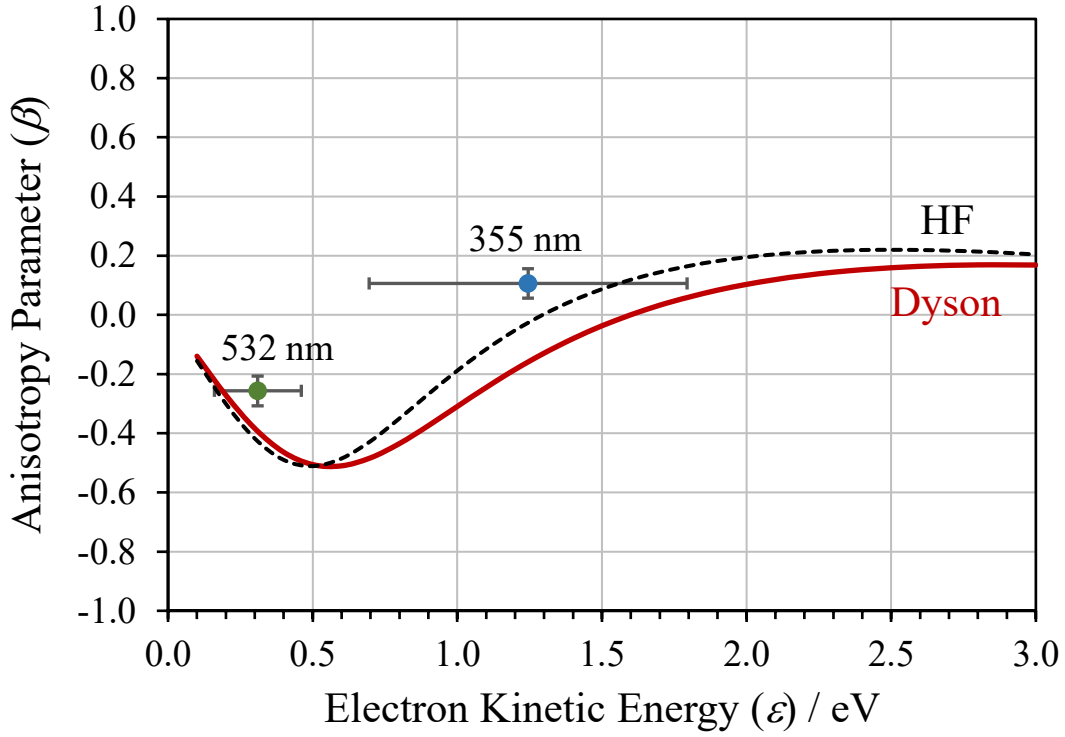

Figure 5. Symbols: the photoelectron anisotropy (β) values determined from the 355 nm and 532 nm experimental data, plotted against the corresponding average eKEs. The large horizontal "error bars" indicate the respective energy ranges over which the PADs were analyzed. The vertical error bars represent the statistical uncertainties in determining the β values. Black dashed and red solid curves: the $\beta(\varepsilon)$ trends predicted by ezDyson based on the HF and Dyson orbitals, respectively, shown in Figure 1.

Figure 6

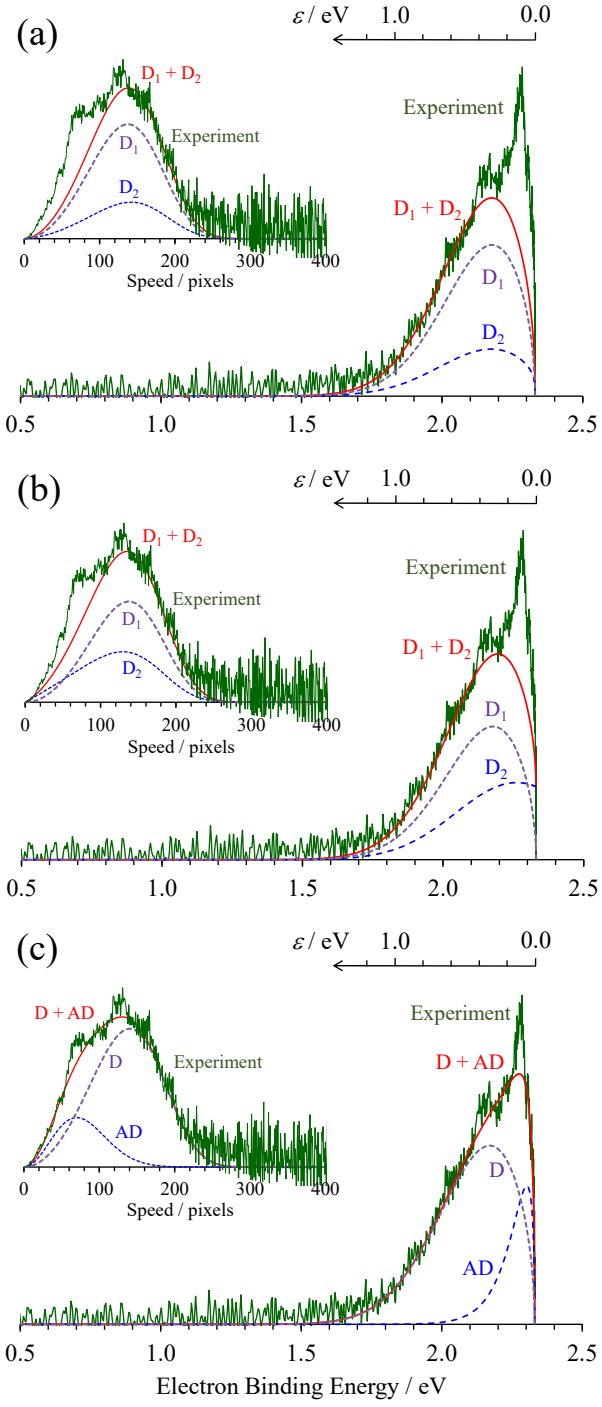

Figure 6. Analysis and modeling of the 532 nm photoelectron spectrum (green) from Figure 4a. In each part a-c of this figure, the 532 nm experimental spectrum is plotted twice: with respect to

eBE (like in Figure 4a) in the main plot and with respect to speed v (proportional to camera pixels) in the inset. The eKE ($\varepsilon = h\nu -$ eBE) scale is also indicated at the top of each main plot. (a) D_1 is the WSG curve for the dominant *trans* anion calculated using model Eq. 2 with P = 0.5, VDE = 2.33 eV, w = 0.22 eV. D_2 is the WSG curve for the *cis* anion calculated using model Eq. 2 with P = 0.29, VDE = 2.26 eV, w = 0.22 eV. $D_1 + D_2$ (red) is the sum of the two model curves representing direct photodetachment of the *trans* and *cis* anions combined, with the normalization constant ratio set in proportion to the expected populations, N_1/N_2 = 0.85/0.15 (Section 4). (b) Similar to (a), D_1 is the WSG curve for the dominant *trans* anion calculated using model Eq. 2 with P = 0.5, VDE = 2.33 eV, w = 0.22 eV. D_2 is the WSG curve for the *cis* anion calculated using model Eq. 2 with P = 0, VDE = 2.26 eV, w = 0.22 eV. $D_1 + D_2$ (red) is the sum of the two model curves, with the normalization constant ratio set to N_1/N_2 = 0.85/0.15, similar to (a). (c) D is the WSG curve for the dominant *trans* anion calculated using model Eq. 2 with P = 0.5, VDE = 2.33 eV, w = 0.23 eV. AD is the model curve representing autodetachment, calculated using Eq. 4, assuming T_{TE} = 630 K. D + AD (red) is the combined model curve. It is reproduced in Figure 4c.

Figure 7

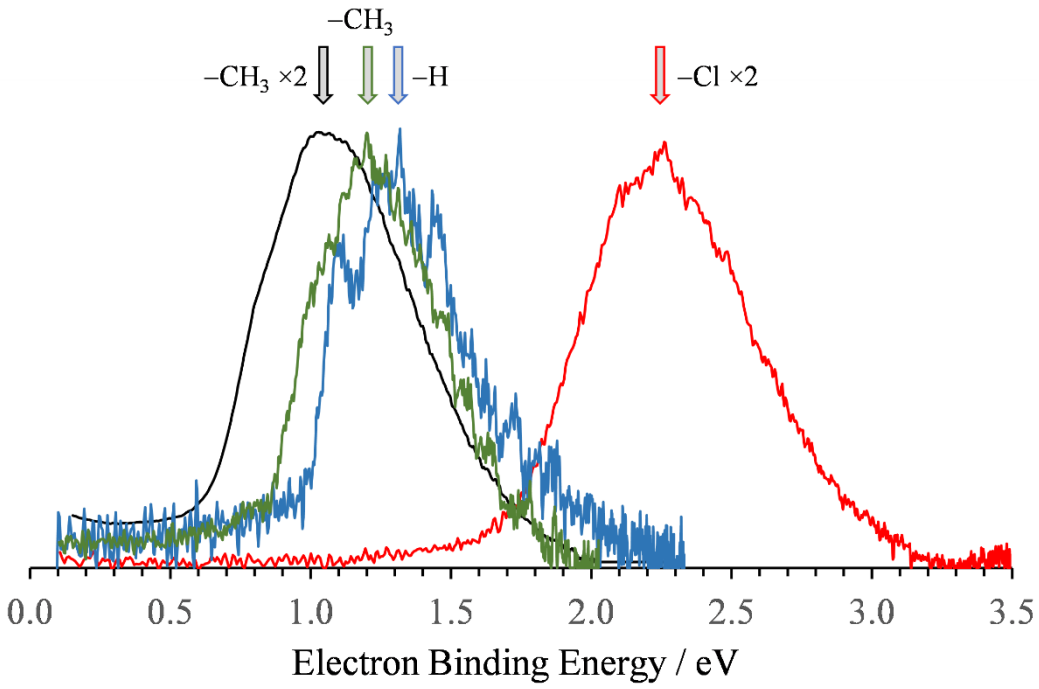

Figure 7. Comparison of the anion photoelectron spectra of (left to right) biacetyl (532 nm), methylglyoxal (612 nm), glyoxal (532 nm), and oxalyl chloride (355 nm). Block arrows above the spectra indicate the respective substituents: –CH_3 (×2) in biacetyl, a single –CH_3 group in methylglyoxal, –H (i.e., no substitution) in glyoxal, and –Cl (×2) in oxalyl chloride.

TOC graphic